THE JOURNAL OF PHYSICAL CHEMISTRY C

Article

pubs.acs.org/JPCC

$ZnWO_4/WO_3$ Composite for Improving Photoelectrochemical Water Oxidation

Kevin C. Leonard, Ki Min Nam, Heung Chan Lee, Soon Hyung Kang, Hyun S. Park, and Allen J. Bard*

Center for Electrochemistry, The University of Texas at Austin, Department of Chemistry and Biochemistry, 105 East 24th Street Stop A5300, Austin, Texas 78712-1224, United States

Supporting Information

ABSTRACT: A rapid screening technique utilizing a modified scanning electrochemical microscope has been used to screen photocatalysts and determine how metal doping affects its photoelectrochemical (PEC) properties. We now extend this rapid screening to the examination of photocatalyst (semiconductor/semiconductor) composites: by examining a variety of $ZnWO_4/WO_3$ composites, a 9% Zn/W ratio produced an increased photocurrent over pristine WO_3 with both UV and visible irradiation on a spot array electrode. With bulk films of various thickness formed by a drop-casting technique of mixed precursors and a one-step annealing process, the 9 atomic % $ZnWO_4/WO_3$ resulted in a 2.5-fold increase in the photocurrent compared to pristine WO_3 for both sulfite and water oxidation at +0.7 V vs Ag/AgCl. Thickness optimization of the bulk-film electrodes showed that the optimum oxide thickness was ~1 μm for both the WO_3 and $ZnWO_4/WO_3$ electrodes. X-ray diffraction showed the composite nature of the WO_3 and $ZnWO_4$ mixtures. The UV/vis absorbance and PEC action spectra demonstrated that WO_3 has a smaller band gap than $ZnWO_4$, while Mott−Schottky analysis determined that $ZnWO_4$ has a more negative flat-band potential than WO_3. A composite band diagram was created, showing the possibility of greater electron/hole separation in the composite material. Investigations on layered structures showed that the higher photocurrent was only observed when the $ZnWO_4/WO_3$ composite was formed in a single annealing step.

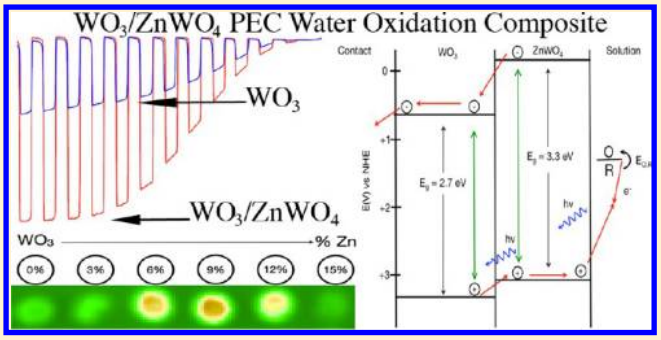

1. INTRODUCTION

We demonstrate that a $ZnWO_4/WO_3$ composite material has a 2.5-fold higher photoelectrochemical (PEC) response for water oxidation than pristine n-type WO_3. Creating efficient n-type photocatalysts for water oxidation has an important role in the wide-scale adoption of renewable energy. This is because the utilization of solar energy requires not only its capture and conversion but also cost-effective energy storage in order for it to be a primary energy source for society.[1] One method for the storage of solar energy is the use of artificial photosynthesis to convert solar energy into storable chemical energy.[2,3] Research in using PEC water splitting to convert solar energy into chemical energy has been very popular since TiO_2 was first suggested as a water splitting photocatalyst in 1972 by Fujishima and Honda.[4] There are many suggested configurations for PEC water splitting, from the simple single-band-gap photoanode configurations, to dual semiconductor or Z-scheme systems, or even integrating solid state photovoltaics into PEC systems ("buried junctions") to provide an additional bias.[5−8] However, a main requirement of all of these systems is an efficient n-type photocatalyst which, when coupled to a suitable oxygen evolution reaction (OER) catalyst, can carry out the four-electron transfer reaction. A large number of n-type semiconductors have been investigated;[9] e.g., WO_3 has been the topic of various PEC studies because it has some promising characteristics such as a band gap (2.7 eV) that can utilize a portion of the visible spectrum and a valence band edge that is positive enough to provide a sufficient driving force to evolve oxygen.[10−13]

Even though WO_3 has these promising characteristics, further improvement in its efficiency as a photocatalyst for water oxidation is still needed. Some of the main methods for improving the PEC response of WO_3 have included morphological improvements and the utilization of nanostructures.[14−23] However, to investigate improving the fundamental properties of photocatalysts (as opposed to morphological properties), rapid screening on doped or composite materials is becoming a useful tool for improving PEC performance.[24] Rapid screening techniques have led to the discovery of new materials to improve many photocatalysts such as Fe_2O_3, $BiVO_4$, and others.[25−27]

In the case of WO_3, McFarland and associates used a rapid screening technique and found that a low concentration of Ni (5−10 atomic %) increased its PEC response.[28] Our group previously found that a compound with a 90:10 ratio of W−Cd resulted in higher photocurrents compared to undoped

Received: April 9, 2013
Revised: July 2, 2013
Published: July 9, 2013

tungsten oxide.[27] In addition to using rapid screening techniques, other methods of changing the chemical composition of WO_3 to improve its PEC water oxidation capabilities have also been reported. Hydrogen treatments of WO_3 have been shown to increase the photocurrent response compared to undoped WO_3.[29] Carbon-doped WO_3 showed an increased photocurrent compared to undoped WO_3 in acidic electrolytes both with and without sacrificial reagents.[30] The use of tungstate materials has also been investigated for PEC oxidation. $ZnWO_4$ and Bi_2WO_6 have been shown to photocatalytically decompose different dyes,[31−33] and $ZnWO_4$ has been shown to have a small photocurrent response (<20 μA/cm^2) for water oxidation under UV irradiation.[32,34] $CuWO_4$ has also been reported as a successful material that produces a photoresponse for water oxidization[35] and has been combined with WO_3 to form a composite electrode material.[36]

In this study, we performed rapid screening analysis on WO_3 composite materials with a modified scanning electrochemical microscope (SECM) previously demonstrated by our group.[24] We characterized spot arrays of WO_3 photocatalysts modified with various additives in compositions ranging from 0 to 15 atomic %. On the basis of these rapid screening results, we determined that a promising candidate composite material was 9% $ZnWO_4/WO_3$. We characterized both its PEC properties and materials properties in an attempt to understand how the $ZnWO_4$ improves the performance of WO_3.

2. EXPERIMENTAL SECTION

Materials. Fluorine-doped tin oxide (FTO, TEC 15, Pilkington, Toledo, OH) coated glass was used as the substrate for both the spot array electrodes and the bulk film electrodes. $(NH_4)_6H_2W_{12}O_{40}\cdot xH_2O$ (≥99.0% Sigma-Aldrich) and $Zn(NO_3)_2\cdot 6H_2O$ (98% Sigma-Aldrich) were used as the metal precursor salts and used as received. In addition, Na_2SO_4, Na_2SO_3, Na_2HPO_4, NaH_2PO_4, NH_4OH, HNO_3, and ethylene glycol (Fisher Scientific) were also used as received. Deionized Milli-Q water was used as the solvent in electrochemical experiments.

Preparation of Photocatalyst Spot Array Electrodes. Spot array electrodes (an electrode composed of spots with each spot having a different composition) were fabricated using the previously reported method.[24] Here, they were fabricated with a CH Instruments model 1550 dispenser (Austin, TX) with a piezoelectric dispensing tip (Micro Jet AB-01-60, MicroFab, Plano, TX) connected to an *XYZ* stage driven by a computer-controlled stepper-motor system (Newport). The FTO substrate electrode was cleaned with soap, Milli-Q water, and ethanol and then sonicated in ethanol for at least 30 min. Before dispensing, FTO substrates were allowed to dry at room temperature in air for at least 12 h. Metal precursor solutions (0.1 M atomic concentrations in ethylene glycol) were dispensed on the FTO substrate to create the spot array electrode. This was done by moving the piezo-dispensing tip to a programmed position over the FTO substrate, and dispensing drops (~100 pL/drop) of the precursor solution by applying a potential of 80 V for 45 μs to the piezo-dispensing tip. The tungsten precursor solution was dispensed first in a preprogrammed pattern onto the FTO substrate, followed by a second metal precursor solution dispensed onto the FTO in an overlay pattern. The distance between photocatalyst spots on the array was about 900 μm with a spot diameter of approximately 500 μm. Each spot had a total of 33 drops, and the spot composition is reported as the relative number of drops of each precursor solution. In all cases, the composition of the second metal was controlled from 0 to 15 atomic % metal-to-tungsten ratio. The prepared arrays were annealed at 500 °C for 3 h (with a 12 h ramp time) in air to form the metal oxide composite materials.

Screening the Spot Array Electrodes. A schematic SECM setup has been described previously.[24] Briefly, a 400 μm diameter optical fiber was connected to a 150 W xenon lamp (Oriel) and was attached to the tip holder of a CHI 900B SECM. The photocatalyst array was used as the working electrode and was placed in the bottom of a specially designed Teflon SECM cell with an O-ring (exposed area: 1.0 cm^2). A Pt wire was used as the counter electrode, and a saturated Ag/AgCl electrode was used as the reference electrode. The electrolyte consisted of 0.1 M Na_2SO_4 and 0.1 M Na_2SO_3 with the SO_3^{2-} used as a sacrificial electron donor. Light from the xenon lamp was passed through the optical fiber, positioned perpendicular to the working electrode ~200 μm above the surface, to illuminate one spot on the working electrode at a time. The optical fiber tip was scanned across the spot array electrode with a scan rate of 500 μm/s, while a potential of +0.2 V vs Ag/AgCl, which is ~300 mV more positive than the onset potential for sulfite oxidation, was applied to the working electrode through the SECM potentiostat. Scanning over the spot arrays revealed two-dimensional images indicative of the generation of photocurrent on each spot. In addition, a 420 nm long-pass filter (removing the UV portion of the spectrum) was used for visible light only illumination rapid screening experiments.

Preparation of Bulk Film Electrodes. FTO substrates were first cleaned as described above. A drop-casting technique was used to create the bulk film electrodes. Here, 200 μL of a 0.02 M precursor solution in ethylene glycol containing either the WO_3 precursor or the desired concentration of the mixed metal/WO_3 composite precursor was dropped onto the FTO substrate (~1.5 cm × 1.5 cm) using a micropipet. To create samples of various thicknesses, multiple coats of the precursor solution were drop-cast onto the FTO substrate with a drying step of 140 °C in air between coats. To obtain thicknesses of less than ~0.3 μm, the concentration of the precursor solution was decreased to 0.01 M. After drop-casting, the bulk film electrodes were annealed using the same conditions as the spot array electrode unless otherwise noted.

The layered $ZnWO_4/WO_3$ composites were also prepared using a similar drop-casting method. For the sequentially annealed samples, 200 μL of 10 mM $(NH_4)_6H_2W_{12}O_{40}$ (the WO_3 precursor) solution was first drop-cast onto the FTO substrate followed by annealing at 500 °C as described above. Then, 2 mM $Zn(NO_3)_2\cdot 6H_2O$ (the Zn precursor) and 2 mM $(NH_4)_6H_2W_{12}O_{40}$ (the WO_3 precursor) solutions were mixed together in a 1:1 ratio and 200 μL was drop-cast onto the annealed WO_3 electrode, which was annealed a second time as described above. For the simultaneously annealed samples, 200 μL of 10 mM WO_3 precursor solution was first drop-cast onto the FTO substrate followed by a drying step of 140 °C for 30 min. Then, 2 mM Zn and W precursor solutions were mixed together in a 1:1 ratio and 200 μL was drop-cast onto the dried sample followed by a single annealing step at 500 °C.

PEC Characterization of Bulk Film Electrodes. PEC characterization was performed in a specially designed borosilicate glass U-type cell in a three-electrode configuration with the bulk film as the working electrode, a Pt flag counter electrode, and a Ag/AgCl reference electrode. The actual

geometric area of the working electrode exposed in the electrolyte and to light illumination was 0.28 cm^2. The same 150 W Xe lamp (Oriel) was used as the light source in the PEC characterization. The PEC measurements were performed in aqueous solutions of either 0.1 M Na_2SO_4 with 0.1 M Na_2SO_3 as a sacrificial electron donor and a phosphate buffer at pH 7 or 0.1 M Na_2SO_4 with a phosphate buffer for water oxidation at pH 7. In all tests, the intensity of the lamp on the sample was measured to be 100 mW/cm^2 using an optical power meter (1830-C, Newport) with a silicon detector (818-UV, Newport) and an attenuator (OD3, Newport). A 420 nm long-pass filter was used to cut the UV portion of the spectrum and to provide only visible light illumination. A monochromator (Photon Technology International, Birmingham, NJ) was used to obtain the action spectra of photoresponse as a function of wavelength.

Materials Characterization of Bulk Film Electrodes. UV−vis absorption spectra were acquired with a Milton Roy Spectronic 3000 array spectrophotometer (New Rochelle, NY) for wavelengths from 330 to 600 nm. X-ray diffraction (XRD) measurements were performed using a Bruker-Nonius D8 advanced powder diffractometer (Madison, WI) operated at 40 kV and 40 mA with Cu Kα radiation (λ = 1.54 Å). Grazing incidence XRD (GIXRD) with an incidence angle of 0.5° was performed to obtain the diffraction pattern of the thin film electrodes on FTO. The scan rate was 12°/min with 0.02° increments of 2θ from 20 to 90°. The JCPDS diffraction database was used to compare our diffraction patterns to those of known materials. X-ray photoelectron spectroscopy (XPS, Kratos Analytical Company) was used to obtain binding energies of the W 4f, O 1s, and Zn 2p orbitals. This was performed with a monochromatic Al X-ray source with a 180° hemispherical electron energy analyzer. Scanning electron microscopy (SEM) was performed with a Quanta 650 FEG, and energy-dispersive X-ray spectroscopy (EDX) elemental maps were obtained with a Bruker XFlash Detector 5010. A 20 kV electron beam was used for both SEM and EDX measurements.

Surface profile images of the bulk films were obtained using a WYKO surface profiler (Veeco Instruments, Inc.). All images were obtained using the vertical scanning interferometry (VSI) mode[37] with a 5× lens. All imaging and data analysis were performed with the WYKO Vision32 (v. 4.20) software. Prior to all measurements, the surface profiler was calibrated with the WYKO Vision32 autocalibration technique using a calibrated step height standard (VLSI Standards Inc.) which has a 8.407 ± 0.068 μm step etched in silicon. Images were obtained by scanning 5 μm above focus, through focus, to 5 μm below focus unless stated otherwise. In some cases, post processing was used to remove sample tilt by utilizing the WYKO Vision32 term mask feature of the software. To determine the film thickness, a portion of the coating was physically removed (by scratching) to expose the FTO glass underneath, and the height difference between the film and the FTO was measured.

Electrochemical impedance spectroscopy (EIS) was conducted on the bulk film electrodes using an Autolab PGSTAT128N (Metrohm USA, Inc.) to obtain Mott−Schottky plots. The EIS measurements were conducted in a 0.1 M Na_2SO_4 solution with an RMS AC amplitude of 10 mV at each applied potential, and measurements were conducted at three different frequencies: 200, 500, and 1000 Hz.

3. RESULTS AND DISCUSSION

SECM Rapid Screening of WO_3 Composite Materials. The initial objective of this study was to determine if the PEC properties of WO_3 could be improved by the addition of other metal oxides. To accomplish this, we created spot array electrodes consisting of WO_3 with a wide range of other added elements to be screened using SECM. In this study, we focused on added metal levels to WO_3 ranging from 0 to 15 metal/tungsten atomic %. Using the SECM technique described in the Experimental Section, we screened spot array electrodes to determine which metal/WO_3 combinations improved the photocurrent response over WO_3 alone. Table 1 summarizes the general effects of these metal/WO_3 combinations for sulfite oxidation. In Table 1, a positive effect indicates that at some added metal concentration a higher photocurrent was observed compared to the WO_3 alone. A negative effect indicates that these samples resulted in lower photocurrents than the WO_3 sample.

Table 1. Summary of the SECM Rapid Screening Results[a]

M/WO_3 combination
positive effect: Zn, Cu, Au, Pb, Ta, Mg, Ru, Ti, Ca, Ni, Pd
negative effect: Cr, Mn, Fe, Cd, Sb, Ag, Co, Cs, Mo, Sn, Nb, Sr, Li, S

[a]A positive effect indicates that at some dopant concentration a higher photocurrent was observed compared to the undoped WO_3. A negative effect indicates that the doped samples resulted in lower photocurrents than the undoped WO_3 sample.

From these rapid screening results, the addition of Zn to WO_3 resulted in the highest photocurrent improvement under both UV and visible light irradiation, so these compositions were the only ones investigated more thoroughly. A typical example of the SECM results of a Zn/W spot array electrode under both full-UV and visible (>420 nm) irradiation is shown in Figure 1. The colors in Figure 1 represent the photocurrent for sulfite oxidation at an applied potential of +0.2 V vs Ag/AgCl with browns representing higher currents and greens representing lower currents. The spot farthest to the left on the spot array represents pure WO_3, and then moving right, each spot has an increased Zn concentration, as illustrated by the schematic above the SECM image. From the SECM screening, we see that a maximum photocurrent response occurred at a 9% atomic ratio of Zn/W. At this ratio, the full-UV photocurrent of the 9% Zn/W spot was ∼75 nA, whereas the undoped W spot produces a photocurrent of ∼45 nA. A similar result is also seen under visible irradiation where a maximum photocurrent is observed at a Zn/W ratio of 9%. As shown below, the addition of Zn to the WO_3 results in partial conversion of the WO_3 to $ZnWO_4$, leading to a composite of the two materials.

We are aware that small changes in the photocurrent measured from the spot array electrodes can be affected by changes in the light intensity delivered through the fiber optic cable or by small thickness variations of the spots on the array electrode; however, the relative photocurrents for the different spots were reproducible. To demonstrate the reproducibility and verify that 9% Zn/W is an optimum ratio for this composite material, we also show a 3 × 6 spot array electrode in which each column of the array has the same Zn/W ratio (Supporting Information, Figure S1). In each row, the column representing the 9% Zn/W ratio shows the highest photo-

dx.doi.org/10.1021/jp403506q | J. Phys. Chem. C 2013, 117, 15901−15910

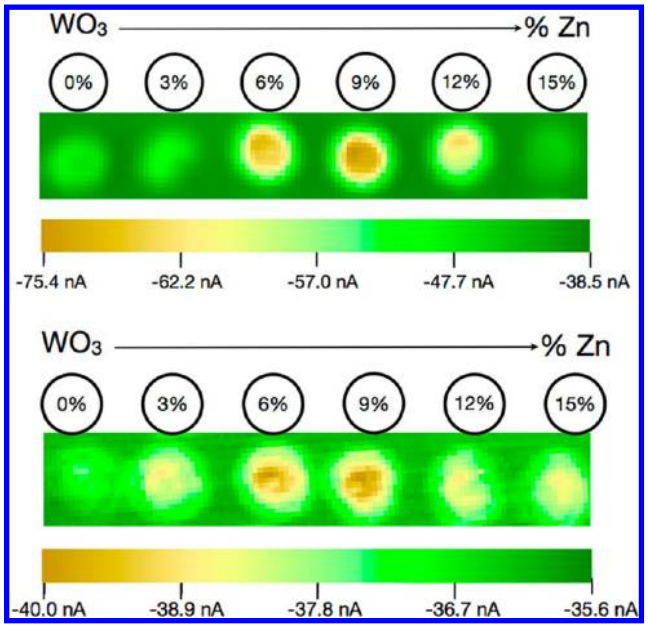

Figure 1. SECM images for the typical photocurrent response of Zn/WO_3 composites (A) under full UV irradiation and (B) with a 420 nm long-pass filter. The color represents the measured photocurrent shown in the scale bar below each SECM image. Also shown is a schematic depicting the percent Zn in each spot in the array electrode. The photocurrent shown is for sulfite oxidation (0.1 M Na_2SO_4 + 0.1 M Na_2SO_3 at pH 7) measured at an applied potential of +0.2 V vs Ag/AgCl.

current response, with the 6% Zn/W ratio showing the next highest response.

PEC Characterization of Bulk-Film Electrodes. To confirm the results of the rapid screening tests that a 9% Zn/W composite showed the highest photocurrent, thin-film bulk electrodes of this composition and of WO_3 alone were created by the drop-casting technique described in the Experimental Section. We compared the PEC activity of WO_3 to 9% Zn/W for both sulfite oxidation (0.1 M Na_2SO_4 + 0.1 M Na_2SO_3 at pH 7) and water oxidation (0.1 M Na_2SO_4 at pH 7) by linear sweep voltammetry (LSV) with chopped light under UV–visible irradiation (Figure 2). In Figure 2, the LSV was conducted from −0.3 to +0.8 V vs Ag/AgCl at a scan rate of 20 mV/s. The film thicknesses for the WO_3 (0.95 μm) and 9% Zn/W sample (0.97 μm) shown in Figure 2 were approximately the same. The 9% Zn/W sample attained at least a 2.5-fold higher photocurrent than the WO_3 for both sulfite and water oxidation. For example, at +0.7 V vs Ag/AgCl, the water oxidation photocurrent of the 9% Zn/W was 0.75 mA/cm^2, while the undoped WO_3 resulted in a photocurrent of 0.27 mA/cm^2. We also observed a more positive onset potential for water oxidation than for sulfite oxidation, consistent with water being more difficult to oxidize than sulfite.

Fill factors were also obtained for both sulfite and water oxidation to determine if the higher photocurrent obtained for the 9% Zn/W sample may result in a smaller fill factor. Using a method reported previously, we estimated fill factors from our three-electrode system using eqs 1–3.[38]

$$P_{optimum} = (E_{sc} - E_{oc})\cdot i_{sc} \quad (1)$$

$$P_{meas} = (E - E_{sc})\cdot i_{photo} \quad (2)$$

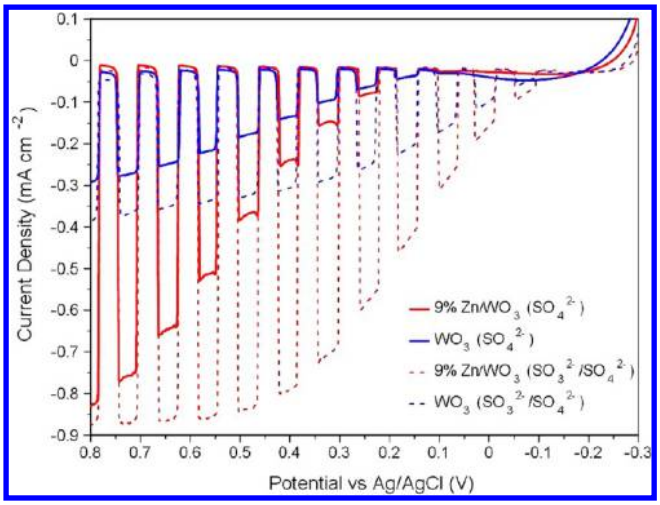

Figure 2. The photoelectrochemical response of bulk film electrodes characterized by linear sweep voltammetry with chopped light under full UV irradiation at 20 mV/s. Shown is the photocurrent for both sulfite oxidation (0.1 M Na_2SO_4 + 0.1 M Na_2SO_3 at pH 7 – dashed lines) and water oxidation (0.1 M Na_2SO_4 at pH 7 – solid lines) for WO_3 and 9% Zn/WO_3. The film thickness was 0.97 μm for the 9% Zn/WO_3 sample and 0.95 μm for the WO_3 sample.

$$FF = P_{max}/P_{optimum} \quad (3)$$

where E_{oc} (open circuit potential) is the potential where photooxidation begins, E_{sc} (short circuit potential) is taken at a potential of 0.8 V vs Ag/AgCl, i_{photo} is the photocurrent at the potential E, i_{sc} is the photocurrent under the defined short circuit conditions, P_{meas} is the power measured at potential E, and P_{max} is taken to be the largest value of the measured power, P_{meas}. The fill factor, FF, is defined as the ratio between P_{max} and the optimum power $P_{optimum}$. The calculated fill factors for the 9% Zn/W and undoped WO_3 were similar both for sulfite oxidation and water oxidation. For sulfite oxidation, the fill factors for the 9% Zn/W and WO_3 samples were 0.41 and 0.39, respectively, while for water oxidation the fill factors were 0.22 and 0.28, respectively. The similar values in fill factor show that the 2.5-fold increase in photocurrent for the 9% Zn/W compared to the undoped WO_3 occurs over a large portion of the potential window, even under low overpotential conditions.

Film Thickness Characterization. To investigate the role of film thickness in the performance of the WO_3 and Zn/W composite electrodes, we created bulk film electrodes of thicknesses ranging from ~0.1 to 1.4 μm. To determine the film thickness, vertical scanning interferometry (VSI) was used as described in the Experimental Section. Figure 3 shows an example of three-dimensional VSI images for three different thicknesses of WO_3. Again, a portion of the coating in each of the three samples was removed to expose the FTO underneath the oxide film and the film thickness was obtained by measuring the height difference between the film and the FTO substrate. The VSI image in Figure 3A is of a relatively thin coating (0.30 μm), and shows good uniformity with almost no cracks or defects. When the film thickness is doubled to 0.63 μm, the film is still uniform but some cracks and defects are now present (Figure 3B). The thickest film of 1.35 μm (Figure 3C) is less uniform, and more cracks and defects are present.

Linear sweep voltammetry under chopped light irradiation was performed on WO_3 and 9% Zn/W films ranging in

dx.doi.org/10.1021/jp403506q | J. Phys. Chem. C 2013, 117, 15901–15910

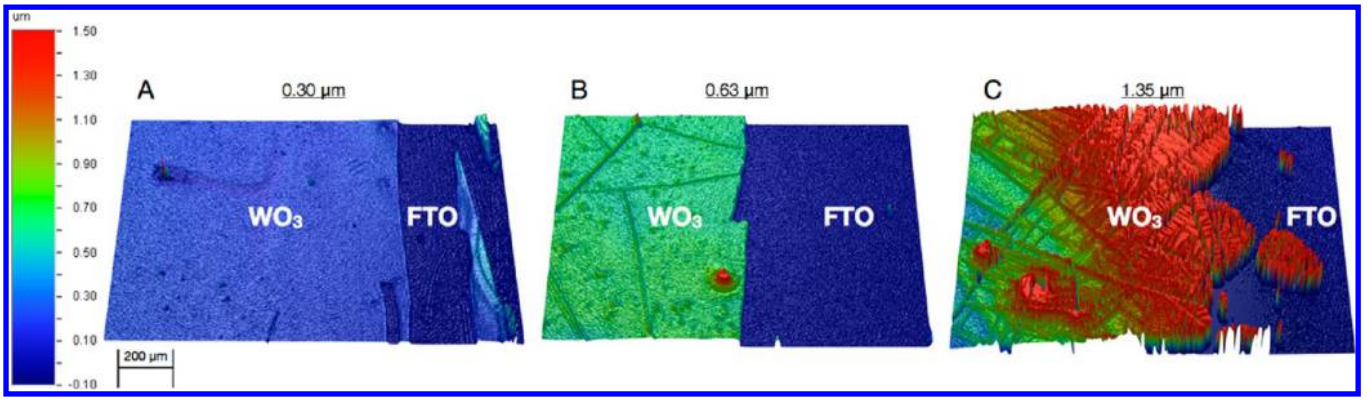

Figure 3. Three-dimensional vertical scanning interferometry images of three different WO_3 samples with thicknesses of 0.30, 0.63, and 1.35 μm. On the right side of each image, the WO_3 film was removed to expose the FTO surface. The height difference between the FTO and the WO_3 was measured to determine the film thickness.

thickness from 0.1 to 1.4 μm. To illustrate how film thickness affects photocurrent, Figure 4 shows the net photocurrent

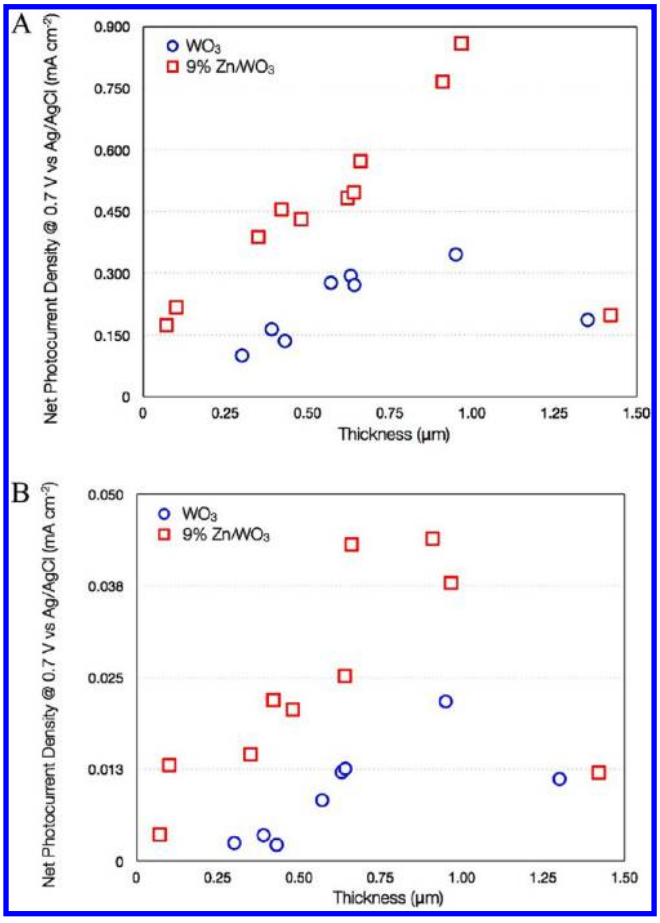

Figure 4. Net photocurrent density as a function of film thickness for WO_3 and 9% Zn/WO_3 at +0.7 V vs Ag/AgCl for sulfite oxidation (0.1 M Na_2SO_4 + 0.1 M Na_2SO_3 at pH 7) under (A) full UV irradiation and (B) visible (>420 nm) irradiation.

(measured current under irradiation subtracting dark current) at +0.7 V vs Ag/AgCl for sulfite oxidation as a function of film thickness for both WO_3 and 9% Zn/W under full-UV (Figure 4A) and visible (>420 nm) irradiation (Figure 4B). The 9% Zn/W films approximately doubled the net photocurrent of the WO_3 over the entire thickness range from 0.1 to 1 μm under both full-UV and visible (>420 nm) irradiation. In addition, the optimum film thickness for both the WO_3 and the 9% Zn/W was approximately 1 μm. Figure S2 in the Supporting Information shows additional examples of the LSV for different thicknesses under UV irradiation (Supporting Information, Figure S2A - WO_3 and 9% Zn/W at ~1 μm; Figure S2B - WO_3 and 9% Zn/W at ~0.6 μm) and a comparison for visible light irradiation (Supporting Information, Figure S2C).

Materials Characterization on Film Electrodes. Characterization of the films demonstrated that the 9% Zn/W was a composite of $ZnWO_4$ and WO_3. XRD measurements were performed on the WO_3 and 9% Zn/W films as described in the Experimental Section (Figure 5). The XRD peak intensities and

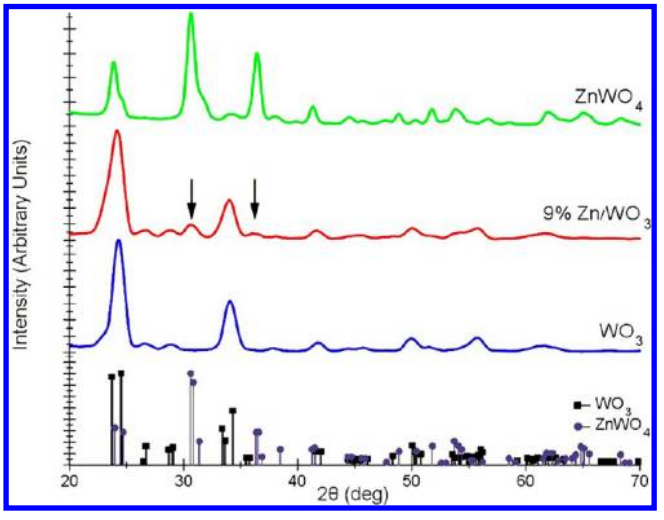

Figure 5. XRD diffraction patterns for the WO_3, 9% Zn/WO_3, and $ZnWO_4$ films on FTO. Also shown are the JCPDS peak intensities and locations for the WO_3 (00-024-0747) and $ZnWO_4$ (00-015-0774).

locations of the WO_3 diffraction patterns match those of monoclinic γ-WO_3[39](JCDPS 00-024-0747). The diffraction pattern of the 9% Zn/W is similar to that of the WO_3 sample; however, two additional peaks occur, highlighted by the arrows in Figure 5. These additional peaks occur at a location (and a relative intensity to each other) where monoclinic $ZnWO_4$ (JCDPS 00-015-0774) displays peaks but WO_3 does not. Thus, the 9% Zn/W is a composite of $ZnWO_4$ and WO_3. To verify that $ZnWO_4$ could be synthesized by a similar drop-casting method, we mixed the Zn and W precursors in a 1:1 ratio of

dx.doi.org/10.1021/jp403506q | J. Phys. Chem. C 2013, 117, 15901−15910

Zn/W and drop-cast them onto an FTO substrate and annealed the sample at 600 °C in air. The XRD pattern of this substrate confirms that $ZnWO_4$ can be synthesized with this method and provides further evidence that the 9% Zn/W sample is a composite of WO_3 and $ZnWO_4$. Structural diagrams showing the lattice parameters of the monoclinic WO_3 and monoclinic $ZnWO_4$ are shown in Figure S3 of the Supporting Information.

XPS measurements were also performed on the WO_3, 9% Zn/W, and $ZnWO_4$ films, and the W 4f, O 1s, and Zn 2p core level peaks are shown in Figure 6. XPS confirms the presence of W and O in all three samples and Zn in the 9% Zn/W and $ZnWO_4$ samples. No significant change in the electronic state of W or Zn in the WO_3, $ZnWO_4$, or 9% Zn/W composite was observed. However, the small shoulder in the oxygen peak that starts to appear in the 9% Zn/W sample and is more noticeable in the $ZnWO_4$ sample may be due to the Zn−O interaction shown in the structural diagram of Figure S3 in the Supporting Information. Also, the atomic ratio of Zn to W in the 9% Zn/W sample was 9 and 91%, respectively, confirming that our composite has a 9% Zn/W ratio.

PEC Characterization of $ZnWO_4$ Films. The materials characterization data suggest that the 9% Zn/W films are composites of WO_3 and $ZnWO_4$. Thus, we compared the PEC performance of $ZnWO_4$ to WO_3 and 9% Zn/W. Figure 7 shows the $ZnWO_4$ PEC activity for water oxidation (0.1 M Na_2SO_4) by LSV under full-UV and visible (>420 nm) light irradiation. The photocurrent for water oxidation with $ZnWO_4$ is more than 2 orders of magnitude lower than either the undoped WO_3 or the 9% Zn/W (Figure 2). Also, unlike WO_3 and 9% Zn/WO_3, $ZnWO_4$ does not show any visible light response. Moreover, the $ZnWO_4$ full-UV photocurrent for water oxidation of 0.02 mA/cm^2 is comparable to values for $ZnWO_4$ previously reported.[34]

Band Gap Characterization of WO_3, 9% Zn/W, and $ZnWO_4$. The observation that $ZnWO_4$ has a much lower photocurrent for water oxidation than WO_3 but a composite of WO_3 and $ZnWO_4$ produces a higher photocurrent for water oxidation than either of the two compounds individually suggests an interesting interaction between the two materials. To investigate whether $ZnWO_4$ changes the band structure of WO_3 when formed into a composite, we obtained the band gap and flat band potentials. The band gaps were found from the PEC action spectra of WO_3, 9% Zn/W, and $ZnWO_4$ to determine the wavelengths for the onset of photocurrent at +0.3 V vs Ag/AgCl (Figure 8). Chopped light with the monochromator adjusted to obtain photocurrents (for sulfite oxidation) at wavelengths at 20 nm intervals was employed. The inset in Figure 8 shows the light intensity through the monochromator at each wavelength. The band gaps of $ZnWO_4$ (3.3 eV) and WO_3 (2.7 eV) are quite different, while 9% Zn/W shows the same onset wavelength as WO_3. The 9% Zn/W composite shows a larger photocurrent at all wavelengths including in the visible region compared to WO_3 itself.

The band gap can also be estimated from the onset of UV−vis absorbance. Figure 9A shows the UV−vis absorbance divided by film thickness for WO_3, 9% Zn/WO_3, and $ZnWO_4$ samples of approximately the same thickness (0.21, 0.20, and 0.25 μm, respectively). Using the absorbance data, Tauc plots were created for each of the three samples (Figure 9B). A Tauc plot can be used to estimate the band gap of a semiconductor because, near the absorption edge, a direct band gap is

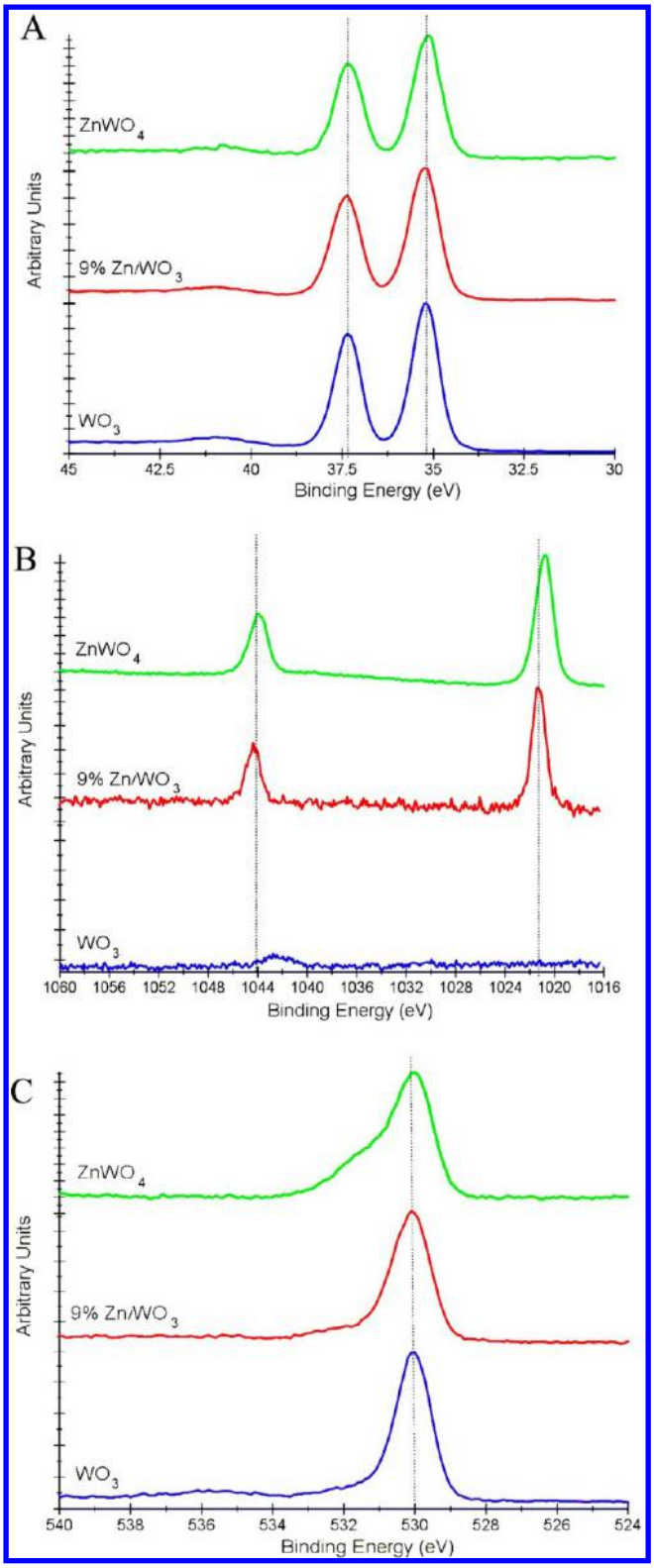

Figure 6. XPS results for of the (A) W 4f, (B) Zn 2p, and (C) O 1s orbitals for samples of WO_3, 9% Zn/WO_3, and $ZnWO_4$.

governed by eq 4, and an indirect band gap is governed by eq 5:[40]

$$\alpha = B_d(h\nu - E_g)^{1/2}/h\nu \quad (4)$$

$$\alpha = B_i(h\nu - E_g)^{2}/h\nu \quad (5)$$

dx.doi.org/10.1021/jp403506q | J. Phys. Chem. C 2013, 117, 15901−15910

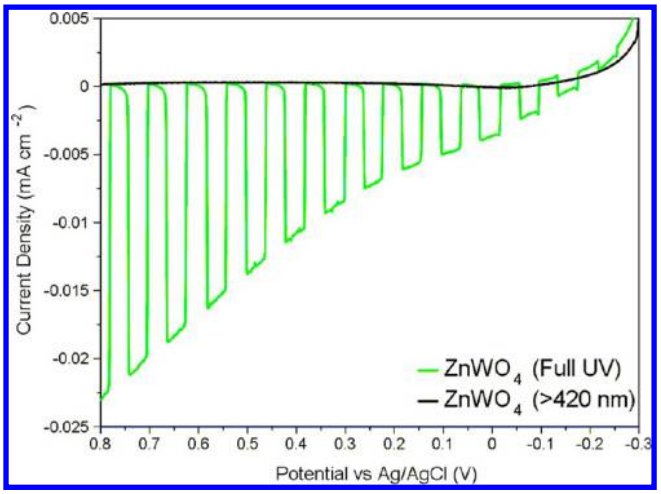

Figure 7. The photoelectrochemical response of a bulk film $ZnWO_4$ electrode characterized by linear sweep voltammetry with chopped light under both full UV and visible (>420 nm) irradiation at 20 mV/s for water oxidation (0.1 M Na_2SO_4 at pH 7).

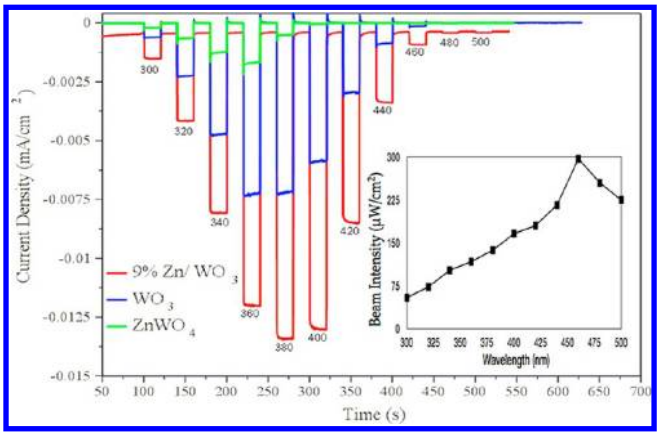

Figure 8. Action spectrum of WO_3, $ZnWO_4$, and 9% Zn/WO_3 for sulfite oxidation (0.1 M Na_2SO_4 + 0.1 M Na_2SO_3 at pH 7) showing the monochromatic wavelength response from 300 to 500 nm at +0.3 V vs Ag/AgCl. The inset shows the light intensity through the monochromator as a function of wavelength.

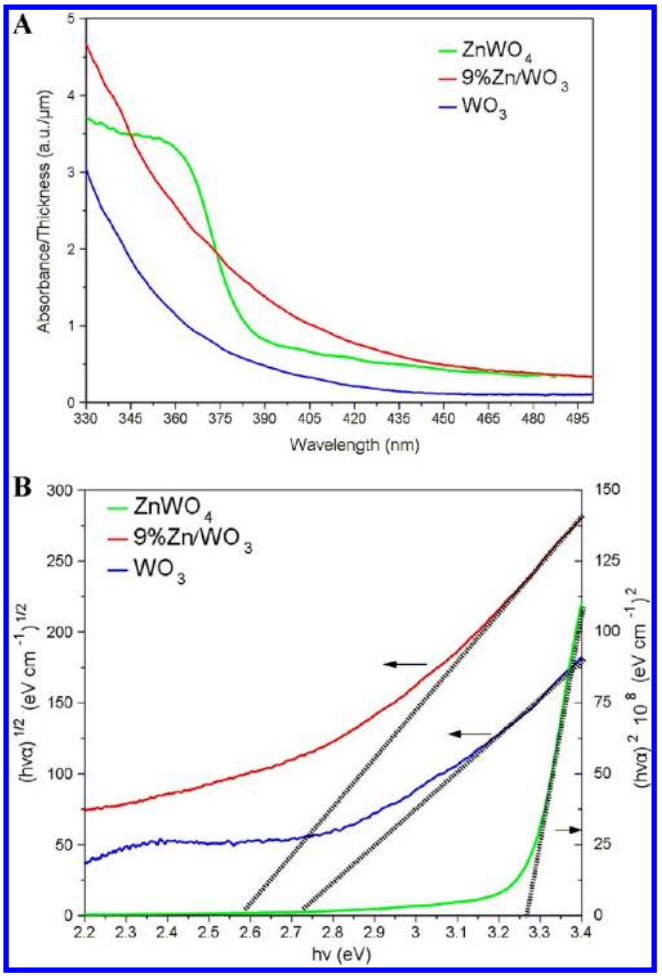

Figure 9. (A) UV–vis absorbance of WO_3 (0.21 μm), 9% Zn/WO_3 (0.20 μm), and $ZnWO_4$ (0.25 μm) divided by oxide thickness as a function of wavelength. (B) Tauc plots of the same WO_3, 9% Zn/WO_3, and $ZnWO_4$ films with the intersection of the dashed (black) line showing the band gap for each sample. The WO_3 and 9% Zn/WO_3 samples were plotted with $(h\nu\alpha)^{1/2}$ vs $h\nu$ for an indirect band gap transition (left axis), while the $ZnWO_4$ sample was plotted with $(h\nu\alpha)^2$ vs $h\nu$ (right axis) for a direct band gap transition.

where α is the absorption coefficient, ν is the frequency, E_g is the band gap energy, h is Plank's constant, and B_d and B_i are absorption constants for direct and indirect transitions, respectively.

From the Tauc plots, the WO_3 and 9% $ZnWO_4/WO_3$ samples showed indirect transitions with band gaps of 2.7 and 2.6 eV, respectively. The pure $ZnWO_4$ sample had a direct transition with a band gap of 3.3 eV. The band gaps obtained from the Tauc plot agree well with the action spectrum data. For additional UV–vis absorbance data, Supporting Information Figure S4 shows the absorbance of samples of various thicknesses of WO_3, 9% Zn/WO_3, and $ZnWO_4$.

Space-charge capacitance data obtained from electrochemical impedance spectroscopy measurements were conducted to obtain Mott–Schottky plots (Figure 10). Using the Mott–Schottky equation at 298 K,[41] we can determine the flat band potential of each semiconductor material. An estimate of the flat band potential was found from the x-intercept of the linear portion of the Mott–Schottky data. An average of the x-intercepts, at three different frequencies, produces flat band potentials for WO_3 and $ZnWO_4$, which were determined to be 0.64 and −0.17 V vs NHE, respectively, with an estimated precision of ±0.1 V. As is frequently the case, flat band potentials obtained from the Mott–Schottky plots show a frequency dependency that may originate from surface roughness or from the many grain boundaries that exist in the drop-cast semiconductor films.

Band Structure Characterization. As described above, the XRD measurements show that, when the W and Zn precursors are mixed, drop-cast, and annealed, they spontaneously form WO_3 and $ZnWO_4$. Since this composite material shows better PEC water oxidation performance than either component individually, we investigated how the band structures of these two semiconductors relate to each other. Using the band gaps obtained from the action spectra and Tauc plots, along with the flat band potential and donor density obtained from the Mott–Schottky experiments, we were able to obtain a schematic of the band energies of a $WO_3/ZnWO_4$ composite.

Figure 11 shows the schematic of the conduction and valence band positions for a $WO_3/ZnWO_4$ composite structure. From the PEC data, $ZnWO_4$ is only active in the UV portion of the spectrum, and much less photoactive than WO_3. However,

dx.doi.org/10.1021/jp403506q | J. Phys. Chem. C 2013, 117, 15901–15910

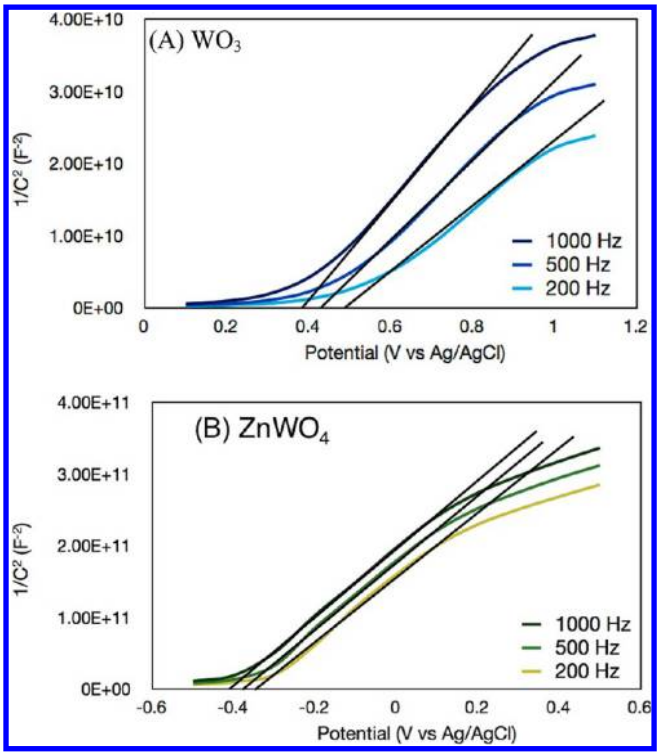

Figure 10. Mott–Schottky plots at frequencies of 200, 500, and 1000 Hz for (A) WO_3 and (B) $ZnWO_4$ in 0.1 M Na_2SO_4 at pH 7 obtained from electrochemical impedance spectroscopy. The *x*-intercept of the linear region (black lines) shows the measured flat-band potential.

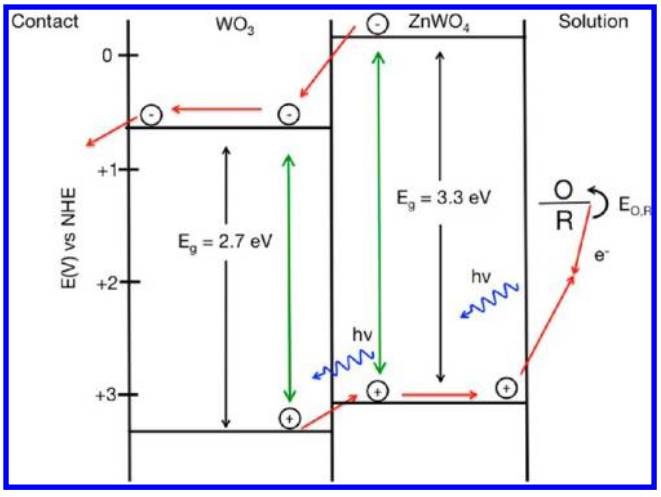

Figure 11. Schematic showing the band diagrams of a $WO_3/ZnWO_4$ composite. The composite structure allows for better electron/hole separation due to the difference in band positions between WO_3 and $ZnWO_4$.

when formed into a composite with WO_3, electrons excited into the conduction band of $ZnWO_4$ can transfer into the conduction band of the WO_3 promoting electron/hole separation. Any light not absorbed by the $ZnWO_4$ will then pass into and be absorbed by the WO_3. Similarly, because the valence band edge of the $ZnWO_4$ is at a higher energy than the valence band edge of the WO_3, holes also move from WO_3 into the $ZnWO_4$, again promoting electron/hole separation. Thus, we propose that the $WO_3/ZnWO_4$ composite promotes electron/hole separation in both semiconductors to yield a higher photocurrent than either of the individual semiconductors.

The band structure in Figure 11 suggests that the optimum ordering of the composite would be WO_3 contacting the conductive FTO and $ZnWO_4$ contacting the electrolyte. In our prepared samples, the W and Zn precursors are first mixed and then annealed, resulting in a randomly distributed composite. SEM images and EDX elemental mappings of the $WO_3/ZnWO_4$ composite are shown in the Supporting Information (Figure S5). The SEM image (Figure S5A, Supporting Information) shows the particle nature of the composite, and the EDX elemental mappings (Figure S5B, Supporting Information) show that Zn and W are in fact homogeneously distributed in the lateral directions.

In an attempt to arrange the order of the composite structure, we fabricated the $ZnWO_4/WO_3$ composite by two different methods. In one, we drop-cast the WO_3 precursor, annealed it at 500 °C to form the WO_3, and then subsequently drop-cast the $ZnWO_4$ precursor and annealed a second time to form the $ZnWO_4$ (sequential annealing). In a second method, the WO_3 was drop-cast as before but was only dried at 140 °C before the $ZnWO_4$ precursor was added. Then, both the WO_3 and $ZnWO_4$ were annealed simultaneously at 500 °C (simultaneous annealing). Figure 12 shows the PEC results

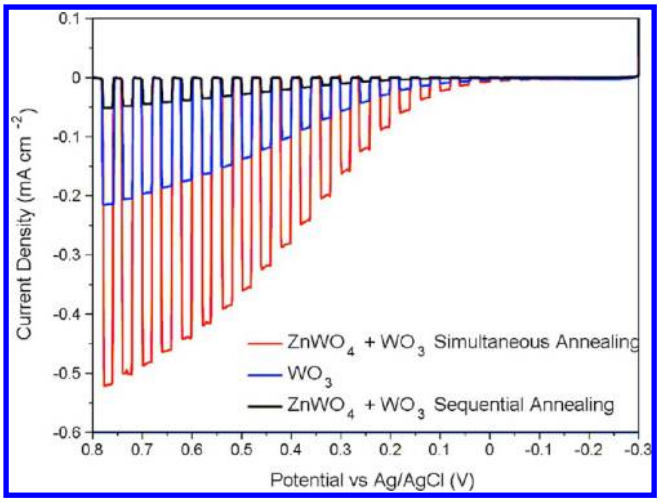

Figure 12. The photoelectrochemical response of bulk film electrodes characterized by linear sweep voltammetry with chopped light under full UV irradiation at 20 mV/s for water oxidation (0.1 M Na_2SO_4 at pH 7) for WO_3 and two 10% $ZnWO_4/WO_3$ samples, one with simultaneous annealing of the $ZnWO_4/WO_3$ and one with sequential annealing of the $ZnWO_4/WO_3$.

for both of these samples along with those of a pristine WO_3 sample synthesized in the same manner. As in Figure 2, where the WO_3 and $ZnWO_4$ precursors were drop-cast and annealed together, the $ZnWO_4/WO_3$ composite material that was simultaneously annealed showed a 2.5-fold increase in photocurrent compared to the pristine WO_3. However, when the WO_3 and $ZnWO_4$ were formed by sequential annealing to produce the same relative composition, the photocurrent was significantly smaller than that of WO_3. Thus, in the simultaneously annealed samples, the order of the semiconductor layers is not highly controllable by this drop-casting technique, because the precursors mix before annealing, resulting in both the WO_3 and $ZnWO_4$ contacting both the electrolyte and the current collector. However, in the

dx.doi.org/10.1021/jp403506q | J. Phys. Chem. C 2013, 117, 15901–15910

Supporting Information (Figure S6), we show both the simultaneous and sequential annealing steps performed in the reverse order ($ZnWO_4$ drop-cast first, followed by the WO_3). As with the initial case, only the simultaneously annealed sample shows an increased photocurrent over pristine WO_3. While the simultaneously annealed sample with the $ZnWO_4$ drop-cast second shows a slightly higher photocurrent than when the WO_3 was drop-cast second, this difference is too small to determine the significance of this improvement.

4. CONCLUSIONS

A PEC modified SECM was used to determine that a 9% Zn/W composite material resulted in a higher photocurrent than pristine WO_3. By synthesizing bulk films of both WO_3 and the 9% Zn/W composite, we determined that the 9% Zn/W composite resulted in over a 2.5-fold increase in photocurrent for both sulfite and water oxidation. By creating films of varied thickness, we were able to make direct comparisons between the 9% Zn/W and pristine WO_3 and determine that the optimum film thickness for both materials was ~1 μm. XRD analysis showed that the 9% Zn/W samples were composites of WO_3 and $ZnWO_4$. PEC characterization revealed that $ZnWO_4$ has a larger band gap and lower photocurrent for water oxidation than WO_3. Mott−Schottky analysis, along with UV−vis absorption and PEC action spectra, allowed us to determine the band structure of a WO_3/$ZnWO_4$ composite. Because of the relative positions of the conduction and valence bands of the two semiconductors, electron/hole separation may be higher in the composite structure than either material individually. In addition, we determined that the increase in photocurrent is only observable when the WO_3 and $ZnWO_4$ were formed by simultaneous annealing.

■ ASSOCIATED CONTENT

Supporting Information

Additional SECM, PEC, UV−vis absorbance, SEM, and VSI data as well as structural diagrams. This material is available free of charge via the Internet at http://pubs.acs.org.

■ AUTHOR INFORMATION

Corresponding Author

*E-mail: ajbard@mail.utexas.edu.

Notes

The authors declare no competing financial interest.

■ ACKNOWLEDGMENTS

We appreciate the assistance of Dr. Shijun Jim Wang and Dr. Sung Ki Cho in obtaining the XPS data and the assistance of Brent Bennett in obtaining the SEM and EDX data. This work was funded by the Division of Chemical Sciences, Geosciences, and Biosciences, Office of Basic Energy Sciences of the U.S. Department of Energy through Grant DE-FG02-09ER16119. K.C.L. would like to acknowledge the Fondazione Oronzio e Niccolò De Nora Fellowship in Applied Electrochemistry.

■ REFERENCES

(1) Lewis, N. S.; Nocera, D. G. Powering the Planet: Chemical Challenges in Solar Energy Utilization. *Proc. Natl. Acad. Sci. U.S.A.* **2006**, *103*, 15729−15735.

(2) Gust, D.; Moore, T. A.; Moore, A. L. Solar Fuels via Artificial Photosynthesis. *Acc. Chem. Res.* **2009**, *42*, 1890−1898.

(3) Bard, A. J.; Fox, M. A. Artificial Photosynthesis: Solar Splitting of Water to Hydrogen and Oxygen. *Acc. Chem. Res.* **1995**, *28*, 141−145.

(4) Fujishima, A.; Honda, K. Electrochemical Photolysis of Water at a Semiconductor Electrode. *Nature* **1972**, *238*, 37−38.

(5) Bard, A. J. Design of Semiconductor Photoelectrochemical Systems for Solar Energy Conversion. *J. Phys. Chem.* **1982**, *86*, 172−177.

(6) Bard, A. J. Photoelectrochemistry and Heterogeneous Photo-Catalysis at Semiconductors. *J. Photochem.* **1979**, *10*, 59−75.

(7) Walter, M. G.; Warren, E. L.; McKone, J. R.; Boettcher, S. W.; Mi, Q.; Santori, E. A.; Lewis, N. S. Solar Water Splitting Cells. *Chem. Rev.* **2010**, *110*, 6446−6473.

(8) Park, H. S.; Lee, H. C.; Leonard, K. C.; Liu, G.; Bard, A. J. Unbiased Photoelectrochemical Water Splitting in Z-Scheme Device Using W/Mo-Doped $BiVO_4$ and $Zn_xCd_{1-x}Se$. *ChemPhysChem* **2013**, DOI: 10.1002/cphc.201201044.

(9) Kudo, A.; Miseki, Y. Heterogeneous Photocatalyst Materials for Water Splitting. *Chem. Soc. Rev.* **2009**, *38*, 253−278.

(10) Seabold, J. A.; Choi, K. S. Effect of a Cobalt-Based Oxygen Evolution Catalyst on the Stability and the Selectivity of Photo-Oxidation Reactions of a WO_3 Photoanode. *Chem. Mater.* **2011**, *23*, 1105−1112.

(11) Xu, Y.; Schoonen, M. A. A. The Absolute Energy Positions of Conduction and Valence Bands of Selected Semiconducting Minerals. *Am. Mineral.* **2000**, *85*, 543−556.

(12) Bak, T.; Nowotny, J.; Rekas, M.; Sorrell, C. Photo-Electrochemical Hydrogen Generation from Water Using Solar Energy. Materials-Related Aspects. *Int. J. Hydrogen Energy* **2002**, *27*, 991−1022.

(13) Sivula, K.; Formal, F. L.; Grätzel, M. WO_3 Fe_2O_3 Photoanodes for Water Splitting: A Host Scaffold, Guest Absorber Approach. *Chem. Mater.* **2009**, *21*, 2862−2867.

(14) Yang, B.; Zhang, Y.; Drabarek, E.; Barnes, P. R. F.; Luca, V. Enhanced Photoelectrochemical Activity of Sol-Gel Tungsten Trioxide Films through Textural Control. *Chem. Mater.* **2007**, *19*, 5664−5672.

(15) Santato, C.; Odziemkowski, M.; Ulmann, M.; Augustynski, J. Crystallographically Oriented Mesoporous WO_3 Films: Synthesis, Characterization, and Applications. *J. Am. Chem. Soc.* **2001**, *123*, 10639−10649.

(16) Qin, D. D.; Tao, C. L.; Friesen, S. A.; Wang, T. H.; Varghese, O. K.; Bao, N. Z.; Yang, Z. Y.; Mallouk, T. E.; Grimes, C. A. Dense Layers of Vertically Oriented WO_3 Crystals as Anodes for Photoelectrochemical Water Oxidation. *Chem. Commun.* **2012**, *48*, 729−731.

(17) Guo, Y.; Quan, X.; Lu, N.; Zhao, H.; Chen, S. High Photocatalytic Capability of Self-Assembled Nanoporous WO_3 with Preferential Orientation of (002) Planes. *Environ. Sci. Technol.* **2007**, *41*, 4422−4427.

(18) Baeck, S. H.; Choi, K. S.; Jaramillo, T. F.; Stucky, G. D.; McFarland, E. W. Enhancement of Photocatalytic and Electrochromic Properties of Electrochemically Fabricated Mesoporous WO_3 Thin Films. *Adv. Mater.* **2003**, *15*, 1269−1273.

(19) Cristino, V.; Caramori, S.; Argazzi, R.; Meda, L.; Marra, G. L.; Bignozzi, C. A. Efficient Photoelectrochemical Water Splitting by Anodically Grown WO_3 Electrodes. *Langmuir* **2011**, *27*, 7276−7284.

(20) Su, J.; Feng, X.; Sloppy, J. D.; Guo, L.; Grimes, C. A. Vertically Aligned WO_3 Nanowire Arrays Grown Directly on Transparent Conducting Oxide Coated Glass: Synthesis and Photoelectrochemical Properties. *Nano Lett.* **2011**, *11*, 203−208.

(21) Liu, X.; Wang, F.; Wang, Q. Screening of Novel Metal Oxide Photocatalysts by Scanning Electrochemical Microscopy and Research of Their Photoelectrochemical Properties. *Phys. Chem. Chem. Phys.* **2012**, *14*, 7894−7911.

(22) Qin, D.-D.; Tao, C.-L.; Friesen, S. A.; Wang, T.-H.; Varghese, O. K.; Bao, N.-Z.; Yang, Z.-Y.; Mallouk, T. E.; Grimes, C. A. Dense Layers of Vertically Oriented WO_3 Crystals as Anodes for Photoelectrochemical Water Oxidation. *Chem. Commun.* **2012**, *48*, 729−731.

(23) Stepanovich, A.; Sliozberg, K.; Schuhmann, W.; Ludwig, A. Combinatorial Development of Nanoporous WO_3 Thin Film Photoelectrodes for Solar Water Splitting by Dealloying of Binary Alloys. *Int. J. Hydrogen Energy* **2012**, *37*, 11618−11624.

(24) Lee, J.; Ye, H.; Pan, S.; Bard, A. J. Screening of Photocatalysts by Scanning Electrochemical Microscopy. *Anal. Chem.* **2008**, *80*, 7445−7450.
(25) Ye, H.; Park, H. S.; Bard, A. J. Screening of Electrocatalysts for Photoelectrochemical Water Oxidation on W-doped $BiVO_4$ Photocatalysts by Scanning Electrochemical Microscopy (SECM). *J. Phys. Chem. C* **2011**, *115*, 12464−12470.
(26) Jang, J. S.; Lee, J.; Ye, H.; Fan, F.-R. F.; Bard, A. J. Rapid Screening of Effective Dopants for Fe_2O_3 Photocatalysts with Scanning Electrochemical Microscopy and Investigation of Their Photoelectrochemical Properties. *J. Phys. Chem. C* **2009**, *113*, 6719−6724.
(27) Liu, W.; Ye, H.; Bard, A. J. Screening of Novel Metal Oxide Photocatalysts by Scanning Electrochemical Microscopy and Research of Their Photoelectrochemical Properties. *J. Phys. Chem. C* **2009**, *114*, 1201−1207.
(28) Baeck, S.; Jaramillo, T.; Brändli, C.; McFarland, E. Combinatorial Electrochemical Synthesis and Characterization of Tungsten-Based Mixed-Metal Oxides. *J. Comb. Chem.* **2002**, *4*, 563−568.
(29) Wang, G.; Ling, Y.; Wang, H.; Yang, X.; Wang, C.; Zhang, J. Z.; Li, Y. Hydrogen-Treated WO_3 Nanoflakes Show Enhanced Photostability. *Energy Environ. Sci.* **2012**, *5*, 6180−6187.
(30) Sun, Y.; Murphy, C. J.; Reyes-Gil, K. R.; Reyes-Garcia, E. A.; Thornton, J. M.; Morris, N. A.; Raftery, D. Photoelectrochemical and Structural Characterization of Carbon-Doped WO_3 Films Prepared Via Spray Pyrolysis. *Int. J. Hydrogen Energy* **2009**, *34*, 8476−8484.
(31) He, D.; Wang, L.; Xu, D.; Zhai, J.; Wang, D.; Xie, T. Investigation of Photocatalytic Activities over $Bi_2WO_6/ZnWO_4$ Composite under UV Light and Its Photo-Induced Charge Transfer Properties. *ACS Appl. Mater. Interfaces* **2011**, *3*, 3167−3171.
(32) Fu, H.; Lin, J.; Zhang, L.; Zhu, Y. Photocatalytic Activities of a Novel $ZnWO_4$ Catalyst Prepared by a Hydrothermal Process. *Appl. Catal., A* **2006**, *306*, 58−67.
(33) Zhang, C.; Zhu, Y. Synthesis of Square Bi_2WO_6 Nanoplates as High-Activity Visible-Light-Driven Photocatalysts. *Chem. Mater.* **2005**, *17*, 3537−3545.
(34) Zhao, X.; Yao, W.; Wu, Y.; Zhang, S.; Yang, H.; Zhu, Y. Fabrication and Photoelectrochemical Properties of Porous $ZnWO_4$ Film. *J. Solid State Chem.* **2006**, *179*, 2562−2570.
(35) Yourey, J. E.; Bartlett, B. M. Electrochemical Deposition and Photoelectrochemistry of $CuWO_4$, a Promising Photoanode for Water Oxidation. *J. Mater. Chem.* **2011**, *21*, 7651−7660.
(36) Yourey, J. E.; Kurtz, J. B.; Bartlett, B. M. Water Oxidation on a $CuWO_4$- WO_3 Composite Electrode in the Presence of $[Fe(CN)_6]^{3-}$: Toward Solar Z-Scheme Water Splitting at Zero Bias. *J. Phys. Chem. C* **2012**, *116*, 3200−3205.
(37) Caber, P. J. Interferometric Profiler for Rough Surfaces. *Appl. Opt.* **1993**, *32*, 3438−3441.
(38) Park, H. S.; Kweon, K. E.; Ye, H.; Paek, E.; Hwang, G. S.; Bard, A. J. Factors in the Metal Doping of $BiVO_4$ for Improved Photoelectrocatalytic Activity as Studied by Scanning Electrochemical Microscopy (SECM) and First-Principles Density-Functional Calculation. *J. Phys. Chem. C* **2011**, *115*, 17820−17879.
(39) Dixon, R.; Williams, J.; Morris, D.; Rebane, J.; Jones, F.; Egdell, R.; Downes, S. Electronic States at Oxygen Deficient WO_3(001) Surfaces: A Study by Resonant Photoemission. *Surf. Sci.* **1998**, *399*, 199−211.
(40) Serpone, N.; Lawless, D.; Khairutdinov, R. Size Effects on the Photophysical Properties of Colloidal Anatase TiO2 Particles: Size Quantization or Direct Transitions in This Indirect Semiconductor? *J. Phys. Chem.* **1995**, *99*, 16646−16654.
(41) Bard, A. J.; Faulkner, L. R. *Electrochemical Methods: Fundamentals and Applications*; John Wiley & Sons, Inc.: New York, 2001.